

# Modular organization of intrinsic connections associated with spectral tuning in cat auditory cortex

Heather L. Read\*, Jeffery A. Winer<sup>†</sup>, and Christoph E. Schreiner\*<sup>‡</sup>

\*W. M. Keck Center for Integrative Neuroscience, University of California, San Francisco, CA 94143; and <sup>†</sup>Department of Molecular and Cell Biology, University of California, Berkeley, CA 94720-3200

Edited by Michael M. Merzenich, University of California, San Francisco, CA, and approved May 1, 2001 (received for review December 14, 2000)

**Many response properties in primary auditory cortex (AI) are segregated spatially and organized topographically as those in primary visual cortex. Intensive study has not revealed an intrinsic, anatomical organizing principle related to an AI functional topography. We used retrograde anatomic tracing and topographic physiologic mapping of acoustic response properties to reveal long-range ( $\geq 1.5$  mm) convergent intrinsic horizontal connections between AI subregions with similar bandwidth and characteristic frequency selectivity. This suggests a modular organization for processing spectral bandwidth in AI.**

corticocortical projections | cortical modules

Little is known about how intrinsic connections in cat primary auditory cortex (AI) are organized and what their functions are. These connections form a discontinuous and elongated spatial pattern (1–3) different from that in the primary visual cortex (4–6). After artificial rerouting of visual thalamic afferents into AI, intrinsic connectivity takes on spatial and functional characteristics of primary visual cortex (VI) (7). However, the relationship between acoustic response properties and intracortical connectivity in AI is unknown. Studies of the spatial organization of frequency (2, 3, 8) and binaurality (8–11) show that these features cannot account for the topography of AI horizontal connections. Injections of AI with anterograde tracers that involve supragranular cortical layers find many intrinsic terminal patches in the dorsoventral (isofrequency) axis and few that cross the caudorostral (cochleotopic) dimension of AI. The frequency preference of the patches was believed to match the injection site because most labeling followed the dorsoventral axis (2, 3). However, it has been suggested that the dorsal patches of labeling are tuned preferentially to higher frequencies (1); hence, the frequency alignment of intrinsic connections in AI is still unresolved. AI neurons also segregate according to binaural properties, and the spatial pattern of excitatory and inhibitory binaural bands covaries with bands of commissural terminal labeling (8–11). However, the spatial arrangement of AI horizontal intrinsic connections differs from that of binaural bands (1).

Features other than characteristic frequency (CF) and binaurality that are represented in AI include intensity dependence, excitatory bandwidth, preferred speed of frequency sweeps, and response latency (12–19). Each feature has a slightly different topographic organization. However, most align dorsoventrally to a central cluster of neurons with narrow bandwidth (NB) tuning (19). This region crosses all frequencies and is flanked above and below (along the isofrequency axis) by clusters of broad-bandwidth (BB) neurons (12, 14, 19). We mapped bandwidth topography (14) to target deposits of a tracer in the central NB region. We found multiple patches of retrograde labeling at consistent and predictable locations within AI. One, and perhaps all, of these patches contain neurons with spectral tuning properties like those of the central NB module. Connections between patches with similar NB tuning properties suggest an

intrinsic system for processing acoustic waveforms with high spectral resolution. The interpatch regions constitute a functionally and anatomically segregated system ideal for broadband spectral processing.

## Methods

**Surgery.** Experiments were conducted on four adult cats by following surgical and recording methods published previously (14). Ketamine (22 mg/kg, i.m.) and acepromazine (0.11 mg/kg) were given before i.v. cannulation. Sodium pentobarbital (15–30 mg/kg, i.v.) was used for surgical procedures including tracheotomy and craniotomy. After exposing AI surgically, sodium pentobarbital was replaced by continuous infusion (i.v.) of lactated Ringer's (1–3 ml/kg per h), ketamine HCl (1–3 mg/kg per h), and diazepam (0.5–2 mg/kg per h) solution.

**Stimulus Control.** Acoustic response properties were acquired in a double-walled sound-attenuating chamber. Stimuli were delivered through STAX-54 headphones connected via a sealed tube into the external acoustic meatus of each ear. The frequency response of this system was flat ( $\pm 6$  dB) up to 14 kHz, which included most of the neurons in this study. Above 14 kHz, the output rolled off at 10 dB/octave.

Sounds were presented at equal sound pressure levels to each ear. Tone bursts (3-ms linear rise and fall; 100-ms total duration; 400- to 1,000-ms interstimulus interval) were generated by a microprocessor (16-bit D–A converter at 120 kHz). Frequency response areas (FRAs) were mapped by presenting 675 pseudorandomized tone bursts at different frequency (range: 3–5 octaves) and sound pressure (range: 5–75 dB) levels. Parylene-coated tungsten microelectrodes with 1–2 M $\Omega$  impedance at 1 kHz were used for single- and multiunit recordings. Recordings in layers IIb and IV (750–1,050  $\mu$ m) were confirmed in two coronally sectioned cases with electrolytic lesions and Nissl staining. Action potentials were isolated from background noise by an on-line window discriminator, and the spike timing was recorded digitally at 10- $\mu$ s resolution.

Boundaries between neighboring auditory fields were delineated by a reversal in the cochleotopic gradient (20) and transitions in receptive field properties besides CF (21, 22). Animals with sulci crossing the 8-kHz isofrequency contour were excluded from the study; the typical sulcal pattern and recording locus is shown in Fig. 1*H*.

This paper was submitted directly (Track II) to the PNAS office.

Abbreviations: AI, primary auditory cortex; BB, broad bandwidth; CF, characteristic frequency; FRA, frequency response area; NB, narrow bandwidth; Q, sharpness of tuning measure; VI, primary visual cortex; WAHG, wheat germ agglutinin apo-horseradish peroxidase colloidal gold.

<sup>†</sup>To whom reprint requests should be addressed. E-mail: chris@phy.ucsf.edu.

The publication costs of this article were defrayed in part by page charge payment. This article must therefore be hereby marked "advertisement" in accordance with 18 U.S.C. §1734 solely to indicate this fact.

**Anatomy.** A NB isofrequency region received an injection of a retrograde tracer, wheat-germ agglutinin apo-horseradish peroxidase colloidal gold (WAHG; ref. 23), in one track at three depths targeting layers III–VI (400–1,400  $\mu\text{m}$ ). A nanoliter injector (World Precision Instruments, Sarasota, FL) was used to make deposits of 5–20 nl/depth through a glass micropipette (tip diameter: 15  $\mu\text{m}$ ). Deposits into layers IV and VI do not produce the patchy pattern of intrinsic label described here (3), although they label thalamic neurons; this served as an independent check on the deposit site. Animals were maintained 3 days more for additional mapping and tracer transport. After recording, electrolytic lesions (Fig. 2 *B–F*, yellow dots) aligned to vascular landmarks were made. Animals were given sodium pentobarbital (150 mg/kg, i.v.) and perfused transcardially with PBS and 4% paraformaldehyde. Cortex was removed, unfolded, flattened, and cut tangentially at 40  $\mu\text{m}$ . WAHG-labeled cells, intensified with silver, were identified and plotted with a NeuroLucida (MicroBrightField, Colchester, VT) system at  $\times 60$ . Plots were rotated and scaled in  $x$  and  $y$  axes to align lesions with physiological maps.

**Physiology.** Four response measures per penetration were derived from the corresponding FRA (13). These are CF, response latency, minimum threshold,  $Q_{10}$ , and  $Q_{40}$  (Fig. 1). Minimum threshold is the sound-pressure level of the quietest tone burst that evokes a response. CF is the tone frequency that evokes a response at minimum threshold. Latency is a measure of the asymptotic minimum of first spike time arrivals across the range of stimulus levels at CF. The difference between lowest ( $f_1$ ) and highest excitatory frequency ( $f_2$ ) of the FRA was a linear measure of bandwidth (BWL) used to derive an index for sharpness of tuning (quality factor,  $Q = \text{CF}/\text{BWL}$ ).  $Q$  values below 0.1 (i.e., bandwidths  $> 5$  octaves) were scored as 0.1;  $Q$  values above 32 (i.e., zero bandwidth) were scored as 32. Response maps were reconstructed by the Voronoi–Dirichlet tessellation (24) in which a polygon is formed by a series of perpendicular lines drawn at halfway points between each recording site and its neighbors (Fig. 1*C*). The size and shape of the polygon are determined by the proximity and positions, respectively, of nearby recording sites. The color of each polygon is the parameter value at the corresponding recording site. This method does not require spatial averaging of the data and is a direct representation of the sampled area. To quantify the  $Q$  or CF values, tessellated maps were interpolated to reduce local scatter in the data while conserving sampling biases (e.g., Fig. 1*D*). Two-dimensional spatial autocorrelograms quantitatively determined the between-peak distances in the  $Q$  maps (Fig. 2*A* and *D*).

## Results

**Multiple Modules for Spectral Integration.** Several AI subregions were identified by their spectral tuning properties. Responses to pure tone stimuli at multiple sound levels were recorded at  $\approx 200\text{-}\mu\text{m}$  intervals across about two octaves of the frequency map in four animals (Fig. 1). This ensured a high-resolution map of CF and  $Q$  for alignment with tracer deposits and labeled neurons. The raw values in the tessellated representation and the reconstructed CF contour map show the expected cochleotopic organization as a gradual color change in the polygons (Fig. 1*C*) and the predicted sequence of isofrequency contours (Fig. 1*D*).

Cortical activation (12, 13, 16, 17) and unit activity (19, 25–27) varied as a function of sound intensity (Figs. 1 and 2). Both  $Q$  and excitatory bandwidth in octaves [ $\text{BW} = \log_2(f_2/f_1)$ ] varied with sound level. Two extremes in  $Q$  intensity dependence were seen in the population and in all cases (e.g., Fig. 1*A* and *B*). Narrow bandwidth FRAs had high  $Q$  values at 10 ( $Q_{10}$ ) and 40 dB ( $Q_{40}$ ) above threshold, whereas BB FRAs had low  $Q_{40}$  values (Fig. 1*A* and *B*). The highest  $Q_{10}$  values were located in the central 2–3

mm of AI (e.g., Fig. 1*E* and *F*, red arrows) whereas lower  $Q_{10}$  values clustered near the dorsal and ventral borders (blue arrows). Frequency histograms for  $Q_{10}$  had a mean of 3 (Fig. 1*G*, red arrow), reflecting the narrow excitatory bandwidths of cells near response threshold.  $Q$  values ranged from 32 to 0.1, corresponding to a BW of 0.04–5 octaves (Fig. 1*G*). Many units were tuned broadly at 40 dB above threshold ( $Q_{10}$  mean =  $3 \pm 2$  vs.  $Q_{40}$  mean =  $1.7 \pm 2$ ; this and subsequent statistical comparisons used the Wilcoxon rank-sum test,  $P < 0.001$ ). This corresponds to a bandwidth difference of  $\approx 1$  octave for 10 vs. 40 dB above threshold ( $\text{BW}_{40}$  mean =  $1.4 \pm 1$  vs.  $\text{BW}_{10}$  mean =  $0.6 \pm 0.4$  octaves). A similar decrease in mean  $Q$  at higher intensities was seen in all cases ( $Q_{10} = 2.4 \pm 2$  vs.  $Q_{40} = 1.2 \pm 2$ ;  $P < 0.001$ ). The unimodal  $Q_{10}$  and  $Q_{40}$  histograms suggest a continuous representation of spectral bandwidth in the population of AI neurons.

Periodic spatial patterns for NB vs. BB units emerged in tessellated  $Q_{40}$  maps (Fig. 2*B* and *E*) and in the spatial autocorrelograms (Fig. 2*A* and *D*). A central cluster of NB neurons with high  $Q_{40}$  factors extended  $\approx 1$  mm across the dorsoventral (isofrequency) axis, designated as the central NB region (14). A second set of NB units lay  $\approx 1.5$  mm dorsal to the central NB region (e.g., Fig. 2*B* and *E*). Each NB region was flanked dorsoventrally by BB unit clusters, creating alternating narrow- and broadband subregions. The spatial periodicity for sharply tuned subregions was quantified by measuring the peak  $Q_{40}$  values at matched CF positions in the spatial autocorrelogram (Fig. 2*A* and *D*). Peaks corresponding to the central and first dorsal NB regions were separated by 1.7 mm ( $\pm 0.39$ , in four animals). NB units were seen  $> 2.5$  mm dorsal; however, this region was not mapped densely enough to assess clustering or to resolve additional autocorrelogram peaks. The minimum corresponding to the first BB subregion was 1 ( $\pm 0.37$ ) mm above the central NB region. Binaural summation, suppression, and null responses all were seen (data not shown) in a single NB cluster, as expected given the high spatial periodicity of binaural interaction bands (8–11).

**Anatomic Modules.** A discontinuous distribution of labeled cells resulted from tracer injection into the central NB region. After establishing the map of spectral tuning across the isofrequency axis, WAHG was injected into the central NB region defined by high  $Q_{10}$  and  $Q_{40}$ . Deposit sites and the dense annulus of labeled neurons filled a region (Fig. 2*C* and *F*, red circles) 795  $\mu\text{m}$  ( $\pm 338$ ) by 730  $\mu\text{m}$  ( $\pm 184$ ). A series of two to three neuron clusters followed the dorsoventral axis above the injection (Figs. 2*C* and *F* and 3*A*). Patchy labeling was confined to superficial layers (600–750  $\mu\text{m}$  below the cortical surface), corresponding to layer III (3). Density peaks were at 1.45 ( $\pm 0.17$ ) mm (d1) and 3.2 ( $\pm 0.08$ ) mm (d3) above the central NB region (Fig. 3*C–F*). Another peak lay 2.4 mm (d2) away in two cases (Fig. 3*C* and *F*). Label in d1 and d2 was within AI; d3 label was on the border of AI and a secondary auditory region, the dorsal zone. The density of neurons labeled in d1 vs. d3 fell from 60% to 10% of the peak value. Thus, most dorsoventral convergence to the central NB region was from neurons  $\approx 1.5$  mm dorsal (d1). Clusters were not found below the injection site, and patches rostral or more than 3.5 mm dorsal were outside of AI, based on frequency gradient reversals. In previous studies, AI intrinsic patches were not always observed or the intervals varied considerably, probably because injections were not placed in identical physiological subregions or layers (1–3).

**Functional and Anatomical Modules Align.** Most labeled neurons were in subregions with NB spectral tuning. The position of labeled neurons relative to the map of  $Q_{40}$  values was determined by aligning physiological maps with flattened sections by using postrecording lesions (Fig. 2*B* and *E*, yellow dots). The first

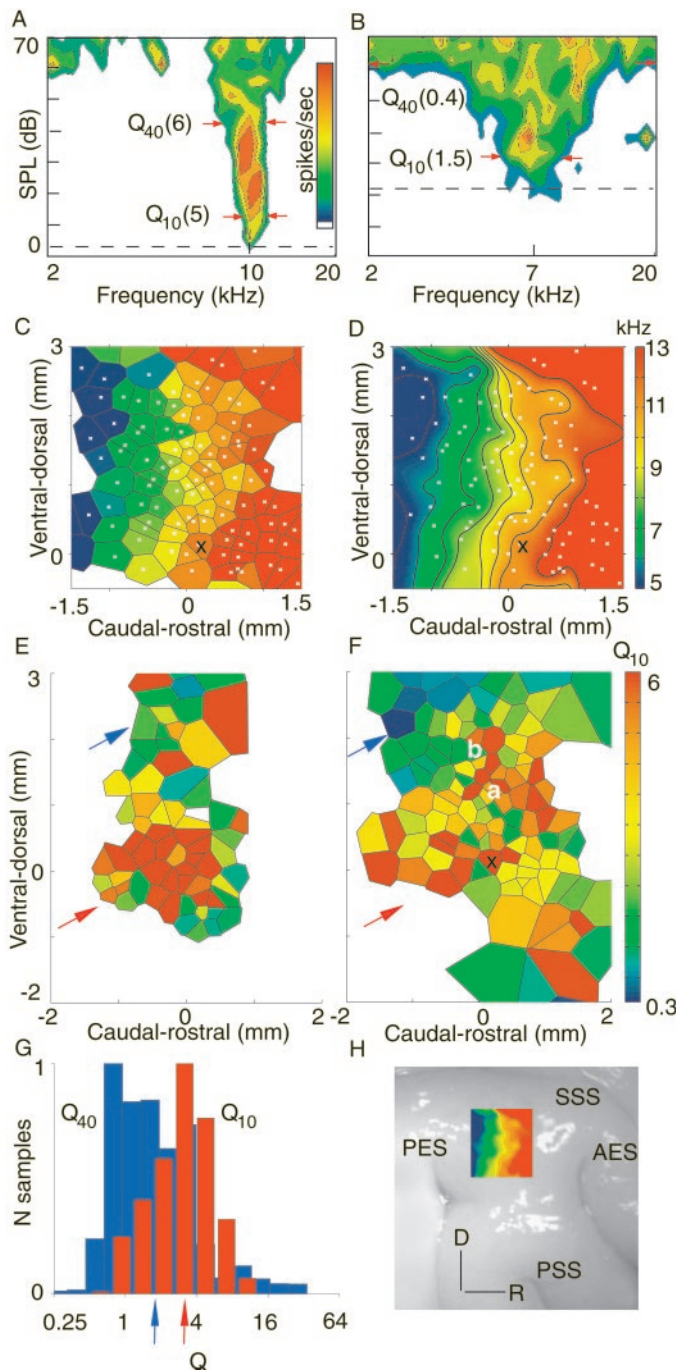


**Fig. 1.** Intensity dependence of frequency tuning in cat AI. (A and B) FRAs for two units from case 119. A has narrow bandwidth at 10 and 40 dB above threshold. B has narrow bandwidth at 10 dB that broadens at higher intensities. Dotted lines, threshold. CF is the preferred frequency at threshold. Lower ( $f_1$ ) and upper ( $f_2$ ) frequency limits, left and right red arrows, respectively, are shown. Color indicates the spikes per second for a 50-msec bin; red corresponds to four spikes/sec in both A and B. Q values are in parentheses. (C) Tessellated CF map. The CF for each track in layers III-IV is assigned to the polygon area without smoothing the data. (D) Isofrequency contour map of CF. Tessellated maps are interpolated before deriving isofrequency contours. White "x" symbols mark individual recording-track positions; black "x" symbols, injection site for case 119. CF (kHz) values are represented with the same color scale in both C and D. The dorsal boundary of AI is  $\approx 2.5$  mm dorsal to the  $x, y = 0, 0$ . The region above  $y = 2.5$  mm is the AI-dorsal zone border. (E and F) Tessellated  $Q_{10}$  maps for cases 510 and 119, respectively. Color spectra in E and F are adjusted so that red represents Q values  $> 4$  and 6, respectively. Loci for FRAs shown in A and B are labeled "a" and "b," respectively in this and subsequent figures. (G) Normalized frequency distributions for  $Q_{10}$  (red bars)

dorsal (d1) patch of neurons (Fig. 2 C and F, white dots/black circles) above the injection site lay within the physiologically defined dorsal cluster of NB AI units. Only 20% of the neurons were in broadband regions with low  $Q_{40}$  values (i.e., those below the mean  $Q_{40}$  for all of AI). In contrast, no spatial relationship was found between the location of label and the  $Q_{10}$  distribution. The alignment of label and NB subcompartments is consistent with the similar peak periodicities ( $\approx 1.5$  mm) observed for the  $Q_{40}$  autocorrelograms (Fig. 2 A and D) and the anatomical histograms (Fig. 3 B-F).

To quantify the overlap between anatomical and physiological clusters, we constructed  $Q_{40}$  density histograms by assigning position-matched  $Q_{40}$  values from the tessellated and interpolated map to each labeled neuron (Fig. 4). Control histograms were made by randomly sampling positions across the entire  $Q_{40}$  map (Fig. 4, blue bars). The mean bandwidth in regions of dense labeling was  $\approx 1$  octave narrower ( $Q_{40}$  2-fold greater) than with sampling across the entire map (blue vs. yellow bars). The high mean  $Q_{40}$  associated with labeled neurons (Fig. 4B, yellow bars) arises primarily from sharply tuned d1 neurons (red bars) and from the central NB region adjoining the injection site. About 80% of labeled neurons (yellow bars) and 70% of those in the d1 patch (Fig. 4, red bars) were associated with  $Q_{40}$  values above the mean for the total area mapped in all cases (Fig. 4B, yellow vs. blue bars;  $P < 0.001$ ). Thus, intrinsic convergence to the central NB region of AI arose mainly from neurons with similarly narrow excitatory bandwidth and high  $Q_{40}$ .

The trajectory of two to three dorsal patches of labeled neurons curved caudally. This deviation could reflect a shift in CF of the projecting cells or a curvature in the isofrequency contours. To resolve these possibilities, neuronal plots were superimposed upon physiological CF maps. Dorsal patches of labeling caudal to the injection site followed the caudal inclination of the isofrequency contour (Fig. 5A). The CF distribution associated with the labeling was quantified by assigning a frequency value from the CF map to each labeled neuron. The frequency distribution within the injection site was estimated by fitting the injection site and halo perimeter with a circle (blue) and taking a random, spatially uniform sample from within the radius. Labeled cells surrounding the injection site extended up to  $\pm 0.7$  octaves ( $\pm 700 \mu\text{m}$ ) in the rostrocaudal frequency axis. In four experiments, the mean CFs for the injection site halo vs. labeled neurons in dorsal AI differed by  $< 0.3$  octaves (Fig. 5 B-D). Cells projecting from as far as 3 mm away in the dorsocaudal direction had CFs matched within  $\pm 0.3$  octaves. Therefore, anatomical convergence from dorsal to central AI links spatially segregated modules matched in CF as well as excitatory bandwidth.

## Discussion

Sound-source discrimination depends critically on the local and global spectral nature of the auditory stimuli (28). Mammals can resolve the frequencies of NB signals, such as pure tones, within fractions of an octave while simultaneously assessing the frequency content of coincident broadband signals, such as background noise, that span several octaves (28, 29). This resolution of pure-tone sources embedded in a noise masker varies with both spectral and temporal features of the masker (28). Thus, broadband, temporally modulated noise maskers permit low-

and  $Q_{40}$  (blue bars) for case 119. The  $Q_{10}$  mean ( $3 \pm 2$ ) was nearly twice that of the  $Q_{40}$  mean ( $1.7 \pm 2$ ,  $P < 0.001$ ). Q values were distributed logarithmically; the Wilcoxon rank-sum test was used for all comparisons. Q ranged between 0.06 and 32; arrows, means. (H) Lateral view of gyri from case 119 and map of CF in a  $3 \times 3.5$ -mm CF map aligned with the approximate recording position. D, dorsal; R, rostral. Sulci: AES, anterior ectosylvian sulcus; PES, posterior ectosylvian sulcus; PSS, pseudosylvian sulcus; SSS, superior sylvian sulcus.

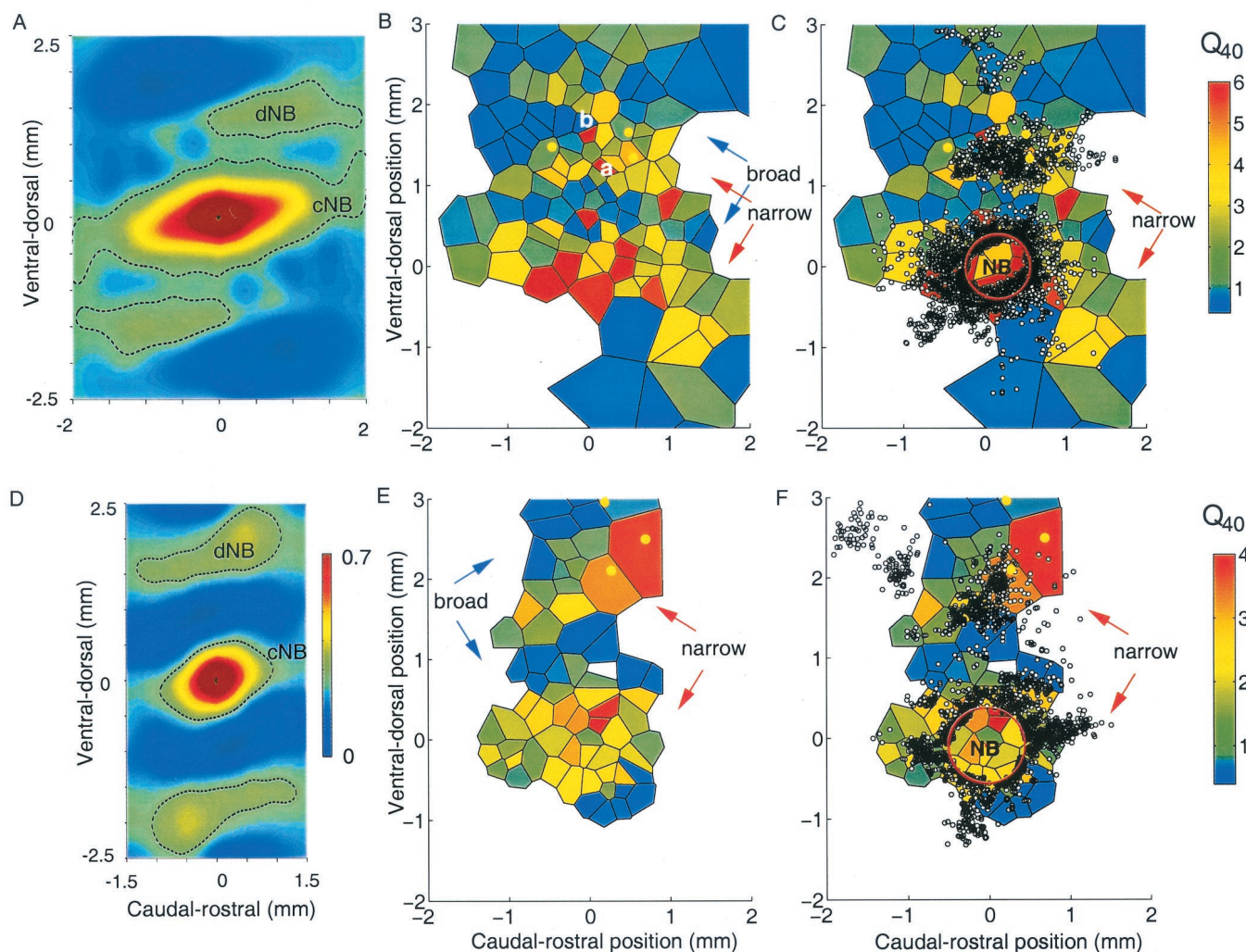


**Fig. 2.** NB units with high  $Q_{40}$  values form two clusters surrounded by clusters of BB units with low  $Q_{40}$  values. The two NB clusters are connected. (A and D) Autocorrelograms from the uniformly sampled region of the tessellated, interpolated  $Q_{40}$  maps in B and E, respectively. Color bars, normalized correlation. (B and E) Tessellated  $Q_{40}$  maps for cases 119 and 510, respectively. Labeling was aligned to the  $Q_{40}$  map with electrolytic lesions (yellow dots). (C and F) Labeling after injections into the central NB region, with deposits centered at 0.0 mm; white dots with superimposed black circles, retrogradely labeled neurons; red circles, deposit and halo in this and subsequent plots. In both examples,  $<30\%$  labeled neurons lay in the BB (blue) subregions between 0 and 2 mm. The lack of correspondence between the map and anatomic label  $>3$  mm dorsal may reflect coarser mapping, occlusion by blood vessels, and lower responsiveness of dorsal AI and dorsal auditory zone neurons.

threshold detection of coincident pure tones, whereas NB or temporally unmodulated noise maskers do not (28). One approach to simultaneous processing of local and global spectral information is to represent these two acoustic dimensions in spatially segregated neural ensembles and to restrict connections to regions with similar functional properties. This predicts that certain types of corticocortical connections ought to be present in auditory cortex. Consistent with this model is the spatially segregated, modular receptive-field organization for spectral bandwidth (Fig. 2). Neurons with high spectral resolution are separated from cells with low spectral resolution (14). Although a direct relationship remains to be established (30), these anatomical modules create a functional dichotomy like that seen psychophysically in critical-band vs. non-critical-band integration behavior (28–30).

We find that the discontinuous intrinsic labeling associated with the central NB region in AI is isofrequency, indicating that a feature other than CF determines this pattern. Further, interconnected anatomic clusters share a common bandwidth, i.e., the central NB cluster is connected primarily to neighboring

and spatially remote NB neurons. Whether analogous links exist between BB subcompartments is uncertain; preliminary data suggest a different intrinsic connection pattern for injections into the ventral BB subcompartment (not shown). NB and BB neurons within the same isofrequency contour should be interconnected if they responded linearly to spectral information alone, because their spectral sensitivities would overlap completely; however, this is not the case. Exclusive connections between similar bandwidth compartments may arise because NB and BB neurons have other contrasting spectrotimporal properties, including the pattern of surround inhibition, intensity dependence, sensitivity to broadband stimuli, and FM sweep selectivities (15, 16, 27, 31, 32). Thus, NB and BB neurons form spatially and functionally distinct modules, and AI intrinsic connections support this segregation.

Is the modular organization of spectral tuning a general feature of vertebrate auditory cortex? Studies in birds (33) and bats (34) find patchy connections between the primary and secondary auditory fields, but there is no evidence for multiple functional or anatomic modules within the isofrequency axis in

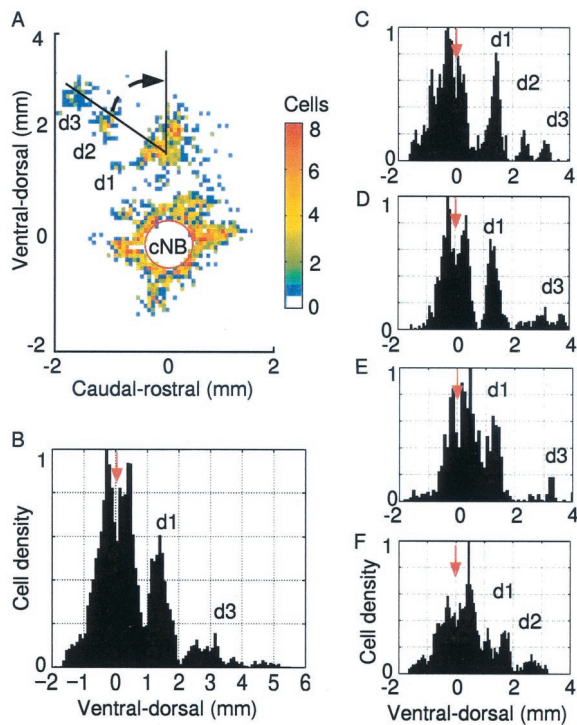


**Fig. 3.** Labeled neurons cluster along the dorsoventral axis of AI after injections in the central NB region (cNB). (A) A two-dimensional density histogram shows their clustered distribution. Color bar, cells/67- $\mu$ m bin. Three dorsal clusters (d1–d3). Labeling above d3 was at the AI border. Dotted white line and arrow, the direction of linear rotation in the two-dimensional histograms in B–F. (B) Data from four animals were pooled and normalized for the population density histogram. One-dimensional density histograms show the periodicity for clusters of labeled cells. All experiments had a dorsal cluster at  $\approx 1.5$  mm (d1). The caudo-rostral-labeling distribution was continuous, unlike that in the dorsoventral axis. (C–F) Density histograms for cases 510, 119, 750, and 440, respectively; each histogram represents one animal. Histograms C and D are from cases in Fig. 2 F and C, respectively.

bird, bat, rat, or ferret AI (24, 33–35). On the other hand, physiological studies of owl (36) and squirrel monkey (37) AI suggest multiple spectral-tuning modules in primates. The AI

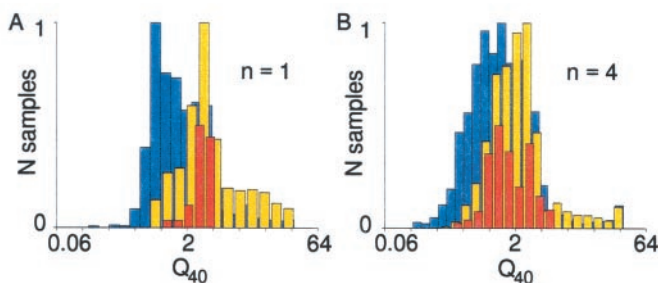


**Fig. 4.** Central NB injections label areas of high  $Q_{40}$ . (A)  $Q_{40}$  density histograms for data in Fig. 2C. The  $Q_{40}$  values for all labeled neurons (yellow bars; mean =  $4 \pm 2$ ) were more than twice that of the  $Q_{40}$  distribution for the entire AI map (blue bars;  $Q_{40}$  mean =  $1.73 \pm 2$ ), which included the broad subregions ( $P < 0.001$ ). Red bars,  $Q_{40}$  histograms for labeling in d1 alone. Eighty percent of all labeling (yellow bars) and 70% of that in the first cluster (d1, red bars) were in high  $Q_{40}$  regions ( $>4$ ). (B) Combined  $Q_{40}$  density histograms for four experiments. The  $Q_{40}$  distribution mean was a little less than twice that for labeled neurons (yellow bars; mean  $Q_{40} = 2.1 \pm 2$ ) than for the entire map (blue bars; mean  $Q_{40} = 1.3 \pm 2$ ,  $P < 0.001$ ). Red bars,  $Q_{40}$  density histograms for the d1 cluster. Labeling outside the mapped areas of AI is excluded from this figure.

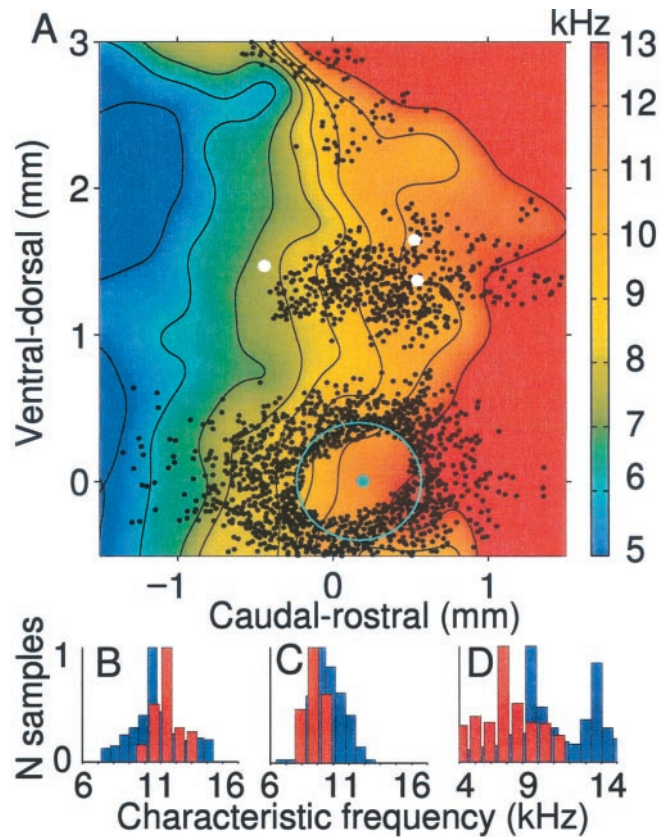


**Fig. 5.** Labeling from central NB deposits is frequency-specific. (A) Labeled clusters and the injection site mapped to a common AI isofrequency contour. (B) A random sample of CFs within the injection site halo was used to assess the CF range in the injection and halo (red histograms). Density histograms show CFs related to dorsal label (blue bars). The mean CF within the halo and the region of dorsal label differed by 0.1 octave in case 119. (C and D) CF distributions from cases 750 and 510, respectively. Larger variations in the frequency distributions for the injection site and labeling reflect sparser mapping (e.g., D); they approached zero with finer mapping (B and C). Larger central injections involved a wider frequency range (D, red distribution). Histograms use a linear frequency scale to highlight differences. The few neurons at the dorsal border of AI were included in the histograms.

isofrequency axis is small ( $<2$  mm) in many species (24, 33–35) relative to that of cat (Fig. 5) and primates (refs. 36 and 37;  $\geq 3$  mm). Modular organization may be too fine to discern with standard methods or absent in species with a small isofrequency representation. Although the idea of spatial segregation by functional parameter (e.g., topographic gradients for best FM sweep rate, binaural integration, and cochleotopy) is valid for all species explored, only some have repeating spatial topographies or modules along the isofrequency axis.

Are the modules in AI organized as those in visual cortex? The 1.7-mm interval between NB subregions approximates the distance between the centers of matched ocular dominance columns in monkey (6, 38) and cat (5, 37) VI. Horizontal projections in VI link columns with common ocular dominance and orientation selectivities (6) and different retinotopic centers for activation (4). Such connections represent functional convergence across retinotopic space. In contrast, the AI dorsoventral intrinsic connections link regions with matched characteristic frequencies and, therefore, cannot represent a large-scale convergence across cochleotopic space (Fig. 5). A NB caudo-rostral or cochleotopic convergence into the central NB region does occur (Fig. 2F) but it is neither long-range nor patchy. Patchy, long-range connections across the isofrequency axis appear in

ferret AI only after developmental manipulation of sensory input (7). The lack of cochleotopic convergence for connections between NB subregions suggests an organizational principle distinct from the convergence across the receptor-surface representation seen in VI.

Anatomic and physiologic metrics indicate that representations of acoustic features in AI can change with altered sensory experience. Novel intrinsic connections across the cochleotopic axis in AI arise with altered sensory input (7). Q distributions change with cochlear lesions (40) and sensory conditioning (24). Accordingly, the relative spatial dimensions of bandwidth modules in AI may be plastic and contingent on experience.

Our finding of an anatomically based functional segregation suggests that the idea of concurrent and independent processing is not limited to specialized domains such as the bat biosonar system (41). Stimulus-specific modularity within a

primary auditory cortical field must precede more global analyses related to sound location (“where”), sound source identification (“who”), and sound meaning (“what”). Such tasks require computational/associative analyses and categorical distinctions across sound structure that likely are not completed at the subcortical level. Their assignment to parallel streams in later cortical stations has been described in primate auditory and frontal cortex (42). How the intrinsic modularity described here contributes to frontal, parietal, or temporal processing streams remains to be seen.

We thank D. T. Larue for histological assistance, and we are grateful to B. H. Bonham, M. P. Kilgard, and M. A. Escabí for contributions to the physiology and analysis. We acknowledge helpful comments by J. F. Linden, L. C. Sincich, J. C. Horton, and D. C. Fitzpatrick. This work was supported by National Institutes of Health Grants 2 R01 DC02260–05 (C.E.S.) and 2 R01 DC02319–21 (J.A.W.).

- Matsubara, J. A. & Phillips, D. P. (1988) *J. Comp. Neurol.* **268**, 38–48.
- Reale, R. A., Brugge, J. F. & Feng, J. Z. (1983) *Proc. Natl. Acad. Sci. USA* **80**, 5449–5453.
- Wallace, M. N., Kitzes, L. M. & Jones, E. G. (1991) *Exp. Brain Res.* **86**, 527–544.
- Bosking, W. H., Zhang, Y., Schofield, B. R. & Fitzpatrick, D. (1997) *J. Neurosci.* **17**, 2112–2127.
- Gilbert, C. D. & Wiesel, T. N. (1989) *J. Neurosci.* **9**, 2432–2442.
- Malach, R., Amir, Y., Harel, M. & Grinvald, A. (1993) *Proc. Natl. Acad. Sci. USA* **90**, 10469–10473.
- Sharma, J., Angelucci, A. & Sur, M. (2000) *Nature (London)* **404**, 841–847.
- Imig, T. J. & Brugge, J. F. (1978) *J. Comp. Neurol.* **182**, 637–660.
- Imig, T. J. & Adrián, H. O. (1977) *Brain Res.* **138**, 241–257.
- Kelly, J. B. & Judge, P. W. (1994) *J. Neurophysiol.* **71**, 904–913.
- Middlebrooks, J. C., Dykes, R. W. & Merzenich, M. M. (1980) *Brain Res.* **181**, 31–48.
- Phillips, D. P., Semple, M. N., Calford, M. B. & Kitzes, L. M. (1994) *Exp. Brain Res.* **102**, 210–226.
- Schreiner, C. E., Mendelson, J. R. & Sutter, M. L. (1992) *Exp. Brain Res.* **92**, 105–122.
- Schreiner, C. E. & Mendelson, J. R. (1990) *J. Neurophysiol.* **64**, 1442–1459.
- Mendelson, J., Schreiner, C. E., Sutter, M. L. & Grasse, K. L. (1993) *Exp. Brain Res.* **94**, 65–87.
- Shamma, S. A., Fleshman, J. W., Wiser, P. R. & Versnel, H. (1993) *J. Neurophysiol.* **69**, 367–383.
- Heil, P., Rajan, R. & Irvine, D. R. F. (1994) *Hearing Res.* **76**, 188–202.
- Mendelson, J. R., Schreiner, C. E. & Sutter, M. L. (1997) *J. Comp. Physiol. A* **181**, 615–633.
- Sutter, M. L. & Schreiner, C. E. (1995) *J. Neurophysiol.* **73**, 190–204.
- Reale, R. A. & Imig, T. J. (1980) *J. Comp. Neurol.* **192**, 265–291.
- He, J. F., Hashikawa, T., Ojima, H. & Kinouchi, Y. (1997) *J. Neurosci.* **17**, 2615–2625.
- Schreiner, C. E. & Cynader, M. S. (1984) *J. Neurophysiol.* **51**, 1284–1305.
- Basbaum, A. I. & Menetrey, D. (1987) *J. Comp. Neurol.* **261**, 306–318.
- Kilgard, M. P. & Merzenich, M. M. (1998) *Science* **279**, 1714–1718.
- Clarey, J. C., Barone, P. & Imig, T. J. (1994) *J. Neurophysiol.* **72**, 2383–2405.
- Irvine, R. F., Rajan, R. & Aitkin, L. M. (1996) *J. Neurophysiol.* **75**, 75–96.
- Suga, N. & Manabe, T. (1982) *J. Neurophysiol.* **47**, 225–255.
- Moore, B. C. J. (1997) *An Introduction to the Psychology of Hearing* (Academic, San Diego).
- Nelken, I., Rotman, Y. & Yosef, O. (1999) *Nature (London)* **397**, 154–157.
- Ehret, G. & Schreiner, C. E. (1997) *J. Comp. Physiol. A* **181**, 635–650.
- Sutter, M. L. & Schreiner, C. E. (1991) *J. Neurophysiol.* **65**, 1207–1226.
- Sutter, M. L., Schreiner, C. E., McLean, M., O'Connor, K. N. & Loftus, W. C. (1999) *J. Neurophysiol.* **82**, 2358–2371.
- Cohen, Y. E. & Knudsen, E. I. (1999) *Trends Neurosci.* **22**, 128–135.
- Fitzpatrick, D. C., Olsen, J. F. & Suga, N. (1998) *J. Comp. Neurol.* **391**, 366–396.
- Owens, A. L., Denison, T. J., Versnel, H., Rebbert, M., Peckerar, M. & Shamma, S. A. (1995) *J. Neurosci. Methods* **58**, 209–220.
- Recanzone, G. H., Schreiner, C. E., Sutter, M. L., Beitel, R. E. & Merzenich, M. M. (1999) *J. Comp. Neurol.* **415**, 460–481.
- Cheung, S. W., Bedenbaugh, P. H., Nagarajan, S. S. & Schreiner, C. E. (2001) *J. Neurophysiol.* **85**, 1732–1749.
- Horton, J. C. & Hocking, D. R. (1996) *J. Neurosci.* **16**, 1791–1807.
- Anderson, P. A., Olvarria, J. & van Sluyters, R. C. (1988) *J. Neurosci.* **8**, 2183–2200.
- Rajan, R. (1998) *Nat. Neurosci.* **1**, 138–143.
- Schreiner, C. E., Read, H. L. & Sutter, M. L. (2000) *Annu. Rev. Neurosci.* **23**, 501–529.
- Romanski, L. M., Tian, B., Fritz, J., Mishkin, M., Goldman-Rakic, P. S. & Rauschecker, J. P. (1999) *Nat. Neurosci.* **2**, 1131–1136.